First Attempt to Observe Velocity Moments in Mössbauer Spectra Measured with Synchrotron Radiation

P. Butkiewicz[a], W. Olszewski[b,*], D. Satuła[b] and K.R. Szymański[b]

[a] *Doctoral School of University of Bialystok, University of Bialystok, K. Ciolkowskiego 1K, 15-245 Białystok, Poland*
[b] *Faculty of Physics, University of Bialystok, K. Ciolkowskiego 1L, 15-245 Białystok, Poland*

Received: 03.07.2025 & Accepted: 28.10.2025

Doi: 10.12693/APhysPolA.148.208 *e-mail: w.olszewski@uwb.edu.pl

We present the application of velocity moment analysis to Mössbauer spectra of single-crystal FeB using synchrotron radiation at BL11XU (SPring-8). This method enables the separation of magnetic dipole and electric quadrupole interactions by analysing first- and second-order velocity moments, independent of nuclear properties. Measurements on FeB single crystals demonstrate the feasibility of this approach, despite challenges from thickness effects.

topics: synchrotron Mössbauer source (SMS), iron monoboride FeB, intensity tensor, velocity moments

1. Introduction

It was demonstrated in [1] that with just a few measurements of a single crystal with a single-site absorber at various orientations of the wave vector relative to the sample, magnetic dipole and electric quadrupole interactions can be separated, and their orientations determined with respect to the sample frame. This approach was made possible by the use of velocity moments, which depend solely on hyperfine fields acting on the nucleus [2], unlike absorption line amplitudes, which depend also on nuclear properties.

The concept described in [1] was not realised in practice. The main difficulty in transmission experiments with a radioactive source is the low counting rate, which limits the possibility of measuring multiple sample orientations. In contrast, a synchrotron source offers a collimated high flux of photons, and energy domain setups [3, 4] and serve as an ideal tool for the measurement of velocity moments.

The significance of this method lies in its capability to disentangle electric quadrupole and magnetic dipole interactions, even when both are present simultaneously. Due to the tensorial character of the velocity moments, the first moment can be represented in the form of a polar diagram to visualize the orientation of the electric field gradient, whereas the second moment is sensitive to magnetic interactions. When measurements are conducted at various sample orientations using unpolarized radiation, this methodology allows for the separate imaging of these interactions. Moreover, the use of circularly polarized radiation enables the determination of the sign of the hyperfine magnetic field. In the ideal case of a single-site absorber, both the orientation of the electric field gradient tensor and the direction of the hyperfine magnetic field can be determined with respect to the crystallographic axes.

Iron–boron-based compounds have recently attracted considerable attention due to their intriguing magnetic properties. Recent theoretical investigations, employing density functional theory (DFT), have offered new insights into the magnetic anisotropy of FeB and related systems. In particular, studies on $(FeCo)_2B$ alloys [5] and boron-doped FeCo thin films [6] have emphasized the influence of band structure and dopant-induced modifications on magnetic anisotropy, thereby reinforcing the potential of FeB-based materials for technological applications. Surface magnetic anisotropy phenomena in $FeBO_3$ have also been explored using crystal field models [7], while recent experimental efforts have systematically characterized spin–orbit interactions in FeCoB nanomagnets [8]. To the best of our knowledge, the canted ferromagnetic order in FeB, as originally proposed by Bunzel et al. [9], has not yet been verified through neutron diffraction measurements.

In this study, we demonstrate the applicability of the velocity moments formalism to single crystals and report the first measurements carried out at the BL11XU beamline at SPring-8 on a single crystal of ^{57}Fe and B.

2. Theoretical framework

The n-th velocity moment W_n of the single-site spectrum measured with unpolarized radiation is defined as

$$W_n = \sum_i v_i^n A_i, \qquad \sum_i A_i = 1. \tag{1}$$

Here, A_i denotes the amplitude and v_i the position of the i-th absorption line. The explicit form of the moments of the spectra was given in [2]. They are constructed from the hyperfine magnetic field $\boldsymbol{B}$, the electric field gradient $\mathbb{V}$, the unit vector $\boldsymbol{\gamma}$ parallel to the wave vector of the incident photon, and the isomer shift δ.

In the present analysis, the focus is only on the first and second moments

$$W_1 = \frac{1}{8}\, a\, \boldsymbol{\gamma}\cdot\mathbb{V}\cdot\boldsymbol{\gamma} + \delta, \tag{2}$$

$$W_2 = b_1\,(\boldsymbol{B}\cdot\boldsymbol{\gamma})^2 + b_2 B^2 + \delta^2 + \frac{1}{2}\, a\delta\, \boldsymbol{\gamma}\cdot\mathbb{V}\cdot\boldsymbol{\gamma} + \frac{1}{24}\, a^2\, \mathrm{Tr}[\mathbb{V}^2], \tag{3}$$

with coefficients

$$a = \frac{e\,Q\,c}{E_0}, \tag{4}$$

$$b_1 = \frac{g_{3/2}\left(-g_{1/2}+3g_{3/2}\right) c\,\mu_N}{4E_0} = 0.005474\,\frac{\mathrm{mm}}{\mathrm{T}^2}, \tag{5}$$

$$b_2 = \frac{\left(g_{1/2}^2-3g_{1/2}\,g_{3/2}+4g_{3/2}^2\right) c\,\mu_N}{4E_0} = 0.01419\,\frac{\mathrm{mm}}{\mathrm{sT}^2}. \tag{6}$$

Here, Q is the nuclear quadrupole moment, e is the elementary charge (positive value), g_I is the nuclear g-factor for spin I, μ_N is the nuclear magneton, E_0 is the energy difference between nuclear states, and c is the speed of light.

The essence of (2)–(5) is that the spectra, expressed in terms of velocity moments as functions of the orientation of the photon wave vector, reveal the pure tensorial characteristics of the hyperfine interactions, independent of explicit nuclear transition probabilities. The use of unpolarized gamma radiation, which effectively averages over photon polarizations, further simplifies the resulting expressions. In practice, spectra often contain multiple sites, each with its own δ, limiting the applicability of (2) and (3).

3. Velocity moments and multicomponent Mössbauer spectrum of single crystal

We propose applying (2) and (3) to components extracted from multicomponent spectra. The spectrum is fitted using octets (full Hamiltonian components), as offered in standard Mössbauer packages, and each component can be analyzed separately with the isomer shift set to zero. This eliminates terms containing δ, making the first velocity moment dependent only on the electric field gradient, while the second moment reflects magnetic texture along with contributions independent of wave vector orientation. The last term in (3) equals $\frac{1}{4}\Delta^2$, where Δ is the absorption line separation for $B = 0$. The proposed isomer shift treatment enables the separation of electric quadrupole and magnetic dipole interactions, revealing the tensor properties of each Mössbauer subspectrum.

In single crystals, applying the velocity moment formalism is less straightforward because crystal symmetries create a range of local electric field gradient orientations. Instead of $\boldsymbol{\gamma}\cdot\mathbb{V}\cdot\boldsymbol{\gamma}$, one observes the symmetry-averaged form $\boldsymbol{\gamma}\cdot\mathbb{V}^*\cdot\boldsymbol{\gamma}$, where $\mathbb{V}^*$ represents the average of $\mathbb{R}_i\,\mathbb{V}\,\mathbb{R}_i^{\mathrm{T}}$ over symmetry operations $\mathbb{R}_i$.

4. Experimental setup

The experiments were performed at BL11XU of SPring-8, Japan, using unpolarized 14.4 keV Mössbauer γ rays produced by a synchrotron Mössbauer source [3]. A diamond phase plate close to the Bragg condition was used as a depolarizer [10]. The source bandwidth was $3.4\Gamma_0$, where Γ_0 is the natural linewidth of the ^{57}Fe nucleus [10]. The γ-ray beam was vertically focused by a Kirkpatrick–Baez mirror. At the focusing position, the vertical and horizontal beam sizes were approximately 30 and 60 μm, respectively. This beam was introduced into the measurement chamber mounted on a 4-axis stage. Additionally, an external magnetic field of 127 kA/m was applied to the crystal to suppress the domain structure and to ensure uniform magnetization within the sample. The transmission Mössbauer spectroscopy spectra were measured using an NaI scintillation detector. The count rate with the sample inserted was approximately 1500–4500 cps. The Doppler velocity scale was calibrated in the usual transmission geometry by using a ^{57}Fe metal foil at room temperature.

5. Sample

The single crystals of FeB were synthesized by melting metallic iron enriched to approximately 95% in the ^{57}Fe isotope and boron in an arc furnace. The bulk samples were annealed, crushed, and crystal grains ranging in size from 20 to 500 μm were selected. The quality of the single crystals was evaluated using X-ray diffraction performed on an Oxford Diffraction SuperNova dual source diffractometer with a monochromatic Mo$K_{\alpha 1}$ X-ray source ($\lambda = 0.70930$ Å). Data collection and

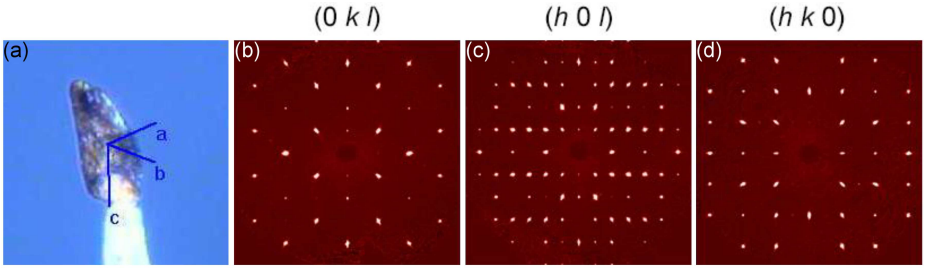

Fig. 1. (a) Oriented single crystal grain of FeB enriched in the ^{57}Fe isotope and (b, c, d) Laue spots in the $(0\,k\,l)$, $(h\,0\,l)$, $(h\,k\,0)$ planes, respectively.

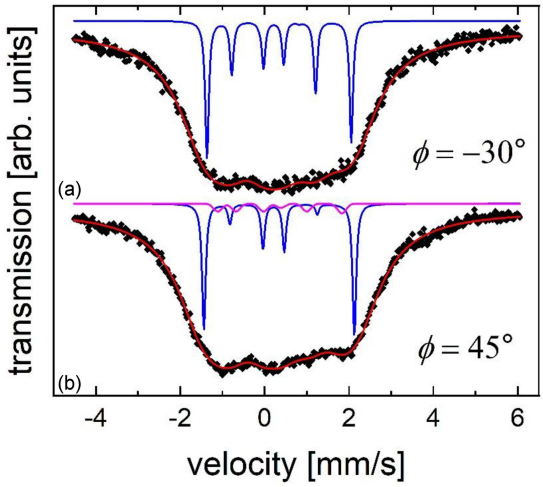

Fig. 2. Two examples from the series of Mössbauer spectra of FeB single crystal. (a) Spectrum is fitted with a single component. (b) Spectrum includes an 18% contribution from a low-field component alongside the dominant one.

processing were carried out using the CrysAlisPro software [11]. The crystal structures were solved by direct methods using SHELXT and refined with SHELXL [12], based on the independent atom model, indicating an orthorhombic P*nma* structure (no. 62 space group). The grain was rigidly glued to the X-ray holder needle, and its orientation was measured by Laue diffraction (see Fig. 1).

6. Results

Twenty-three spectra were collected, and two examples are shown in Fig. 2. Transmission integral fitting was used in the analysis [13, 14]. The significant thickness effect hinders the straightforward interpretation of the hyperfine structure. We performed simulations for the ellipsoidal sample shape with extreme dimensions obtained from optical microscopy (Fig. 1a). After including the beam sizes (30 μm and 60 μm) and the beam direction, the estimated thicknesses for the measurements (Table I) ranged between 1020 and 2200. The thickness distribution was between 10 and 115. Therefore, we attempted to use known parameters of FeB spectra. The spectra of single-crystal and polycrystalline FeB, each consisting of a single sextet, were presented in [15] and [9], respectively, while spectra of polycrystalline samples presented in [16] and [2] show an additional magnetic component, interpreted as the influence of substitutional boron [16].

As the fraction of the additional component is unknown, the spectra were analyzed assuming its contribution to be 0%, 18%, or 26% of the spectral area. When performing the fits, we assumed that for the main FeB component, one obtains $\mathbb{V}_{zz} = -0.459$ mm/s and the asymmetry parameter is $\eta = 0.46$, consistent with the spectra presented in [2]. The orientation of the hyperfine interactions with respect to the wave vector and the thickness parameter were fitted to the spectra.

Although the quality of the fits shown in Fig. 2 is rather good, the extracted values of the velocity moments W_1 and W_2 were influenced by large uncertainties due to the aforementioned thickness effects. Numerical values are presented in Table I. The uncertainties associated with W_1 and W_2 were estimated based on the analysis of independent experiments performed with identical sample orientation relative to the photon wave vector.

7. Discussion

Since FeB crystallizes in the P*nma* space group (no. 62), the electric field gradient (EFG) tensor $\mathbb{V}$ at the Fe site has arbitrary orientation and transforms under the symmetry operations: (x, y, z), $(-x, -y, z)$, $(-x, y, -z)$, $(x, -y, -z)$, and their compositions with inversion.

Let the corresponding rotation matrices be denoted by $\mathbb{R}_i$ $(i = 1, \ldots, 4)$. A direct calculation shows that the averaged tensor

$$\mathbb{V}^* = \frac{1}{4}\sum_{i=1}^{4} \mathbb{R}_i\, \mathbb{V}\, \mathbb{R}_i^{\mathrm{T}} \qquad (7)$$

is diagonal when expressed in the principal axes of the P*nma* space group.

TABLE I

Experimentally obtained values of the velocity moments W_1 and W_2 (columns 4 and 7), along with a comparison to fitted site-averaged values (columns 5 and 8) related to the green surface in Fig. 3 and the red curve in Fig. 4, respectively. The Cartesian coordinates of the $\boldsymbol{\gamma}$ vector in the sample frame, shown schematically in Fig. 1, are presented in columns 1–3. The data in columns 4 and 5 correspond to Fig. 3, while the data in columns 6–8 refer to Fig. 4.

	γ_x	γ_y	γ_z	$W_1 \pm 0.015$ [mm/s]	$W_{1\text{th}}$ [mm/s]	ϕ [deg]	$W_2 \pm 0.11$ [mm^2/s^2]	$W_{2\text{th}}$ [mm^2/s^2]
	1	2	3	4	5	6	7	8
1	0.494	−0.752	0.436	0.094	0.089	−30	2.28	2.73
2	0.984	−0.102	−0.144	0.081	0.087	30	2.33	2.73
3	0.95	0.111	−0.291	0.065	0.082	45	2.35	2.541
4	0.494	−0.752	0.436	0.062	0.089	−30	2.36	2.73
5	0.755	−0.599	0.267	0.096	0.092	−10	2.63	2.221
6	0.926	−0.373	0.065	0.099	0.092	10	2.40	2.221
7	0.984	−0.102	−0.144	0.089	0.087	30	2.15	2.73
8	0.95	0.111	−0.291	0.066	0.082	45	2.33	2.541
9	0.257	−0.808	0.53	0.099	0.085	−45	2.37	2.541
10	0.494	−0.752	0.436	0.083	0.089	−30	2.43	2.73
11	0.984	−0.102	−0.144	0.081	0.087	30	2.27	2.73
12	0.95	0.111	−0.291	0.084	0.082	45	2.19	2.541
13	0.257	−0.808	0.53	0.091	0.085	−45	2.38	2.541
14	0.494	−0.752	0.436	0.11	0.089	−30	2.26	2.73
15	0.755	−0.599	0.267	0.108	0.092	−10	2.26	2.221
16	0.926	−0.373	0.065	0.109	0.092	10	2.32	2.221
17	0.984	−0.102	−0.144	0.103	0.087	30	2.43	2.73
18	0.95	0.111	−0.291	0.104	0.082	45	2.28	2.541
19	0.853	−0.493	0.169	0.099	0.093	0	2.41	1.999
20	0.525	−0.692	0.495	0.102	0.083	–	–	–
21	0.701	−0.643	0.309	0.08	0.092	–	–	–
22	0.237	−0.685	0.689	0.075	0.066	–	–	–
23	0.525	−0.692	0.495	0.095	0.083	–	–	–

A method for reconstructing the averaged tensor $\mathbb{V}^*$ from experimental data is proposed. Since the EFG is a traceless second-order tensor, it surely contains both positive and negative components, which complicates its direct representation using polar plots — unlike, for example, the inertia or diffusion tensors, which form ellipsoids. To circumvent this, the following quantity is considered for plotting

$$\boldsymbol{\gamma} \cdot \mathbb{V}^* \cdot \boldsymbol{\gamma} + \sqrt{\mathrm{Tr}\,(\mathbb{V}^* \cdot \mathbb{V}^*)}, \tag{8}$$

which is a strictly positive function of the unit vector $\boldsymbol{\gamma}$. According to (1), with a sufficient number of measurements performed for various orientations of the wave vector $\boldsymbol{\gamma}$, this representation reflects the shape of $\mathbb{V}^*$, as illustrated by the green surface in Fig. 3.

In the present experiment, the available dataset is limited and exhibits considerable dispersion. Therefore, the surface shown in Fig. 3 corresponds to a fit based on the values reported in Table I (column 5), under the assumption of orthorhombic symmetry and alignment of the principal axes of $\mathbb{V}^*$ with the crystallographic directions.

In the ferromagnetic state, FeB exhibits two magnetically easy axes within the *ab* plane [17]. In the measurement shown in Fig. 4, the external magnetic field was applied partially along the hard *c* direction. Since the saturation field in the easy plane is approximately 160 kA/m [17], full magnetic saturation of the crystal is not expected. Despite this, the experimental data show strong dispersion, and W_2 does not exhibit a systematic dependence on the angle ϕ. Consequently, although W_2 could, in

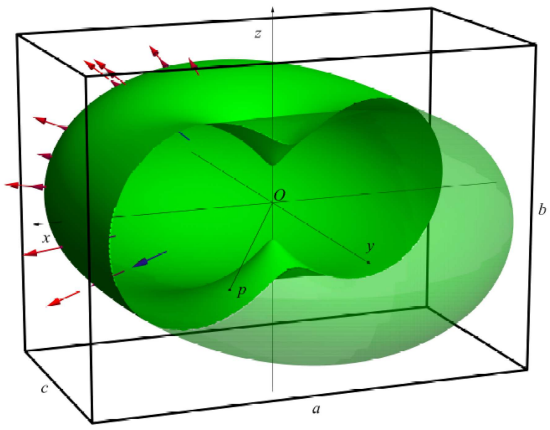

Fig. 3. Comparison of the experimentally determined first velocity moment with theoretical expectations. The green surface represents the theoretical $a\boldsymbol{\gamma}\cdot\mathbb{V}^*\cdot\boldsymbol{\gamma}$ values. The distance from any point p on this surface to the origin O is equal to $(a\boldsymbol{\gamma}\cdot\mathbb{V}^*\cdot\boldsymbol{\gamma}+s)/8$, where $\boldsymbol{\gamma}$ is a unit vector along Op, and $s = a\sqrt{\mathrm{Tr}[\mathbb{V}^2]} = 0.582$ mm/s ensures positivity. Arrows indicate the incident photon wave vector directions, with arrowhead distances from O given by $W_1 + s$, where W_1 is the measured value (Table I, column 4). Red arrows denote $W_1 + s$ exceeding theoretical values, while blue arrows indicate lower values. The orientation of the FeB unit cell frame is shown by a thick line. The radially oriented error bar, shown at the head of the arrow closest to the a edge of the unit cell, is representative and applies uniformly to all arrowheads.

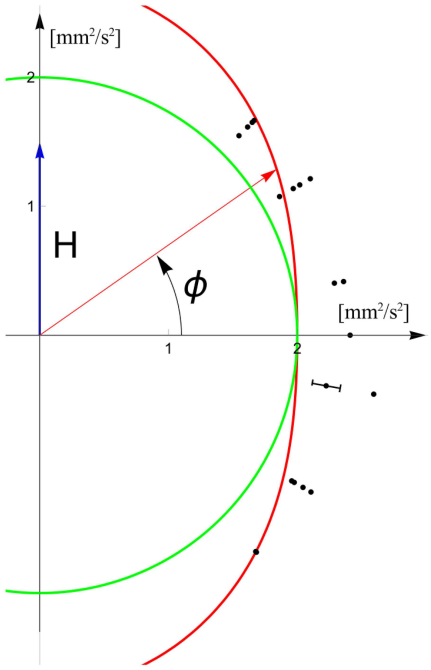

Fig. 4. Comparison of the experimentally determined second velocity moment with theoretical expectations. The red curve represents the theoretical $b_1(\boldsymbol{B}\cdot\boldsymbol{\gamma})^2$ values, with red arrow lengths given by $b_1(\boldsymbol{B}\cdot\boldsymbol{\gamma})^2 + const$, where $\boldsymbol{\gamma}$ is a unit vector along the arrow. The green curve represents the constant value $const = b_2B^2 + \frac{1}{24}a^2\,\mathrm{Tr}[\mathbb{V}^2]$. Black points mark the incident photon wave vector directions, with their distances from the origin corresponding to the measured W_2 values (Table I, column 7). The blue arrow indicates the direction of the applied external magnetic field. The radially oriented error bar, shown for a single data point, is representative and applies uniformly to all data points.

principle, provide insight into the crystal's magnetic state, the present measurements do not allow for such a determination.

The obtained results exhibit significant dispersion. Ideally, the arrowheads in Fig. 3 should lie on a single surface (e.g. the green one), and the black points in Fig. 4 should align along a single curve. The strong dispersion remains not fully understood. One likely contributing factor is the effect of absorber thickness, which can broaden and distort the spectral lines. Variations in thickness across different regions of the single crystal presumably contribute to this effect, leading to an unaccounted distribution of thicknesses in the analysis. For future work, a detailed explanation of the mechanism of the effect of thickness and a quantitative simulation of the data variability are essential.

Attempts to use smaller single crystals were hindered by the beam size, which exceeded the crystal dimensions, resulting in poor spectral statistics. Additionally, fitting with different contributions (0%, 18%, 26%) of the second, low-field component did not improve the regularity of the velocity moments. To evaluate the sensitivity of the velocity moments to such compositional variations, a Monte Carlo analysis is required.

Future experiments are expected to yield reliable results by using precisely enriched ^{57}Fe single-crystal absorbers with optimized thickness, in combination with a microfocus synchrotron beam delivering a smaller spot size.

8. Conclusions

The extension of the velocity moments formalism, originally introduced for a single-site system, to single crystals with characteristic symmetries and multicomponent spectra has been demonstrated. The first and second velocity moments of a subspectrum reflect its tensor properties and enable the separation of magnetic dipole and electric quadrupole interactions. The first moment reflects crystal symmetry, while the second moment captures the angular distribution of the hyperfine magnetic field, which is closely linked to macroscopic magnetization. We have demonstrated how to separate magnetic dipole

and electric quadrupole contributions in the case of mixed interactions from spectra of a crystal showing the presence of several orientations of local environments related to crystal symmetries. Unfortunately, the experimental precision of this first attempt was not fully satisfactory.

Future work will focus on the preparation of samples with a smaller effective thickness and enhanced uniformity to improve spectral resolution.

Acknowledgments

The synchrotron radiation experiments were performed using a QST experimental station at the QST beamline BL11XU, SPring-8, with the approval of the Japan Synchrotron Radiation Research Institute (JASRI) (SPring-8 Proposal No. 2022B3582 under the ARIM program JPMXP1222QS0102). We would like to thank Dr. Takaya Mitsui for fruitful discussions, Dr. Mitsui and Dr. Kosuke Fujiwara for their assistance with data collection, and Szymon Zubrzycki for 3D-printing the sample holder.

This work was partially supported by the National Science Centre (Grant No. OPUS 2018/31/B/ST3/00279).

References

[1] K.R. Szymański, *Eur. Phys. J. B* **91**, 292 (2018).

[2] K. Szymański, *Phys. Rep.* **423**, 295 (2006).

[3] T. Mitsui, N. Hirao, Y. Ohishi, R. Masuda, Y. Nakamura, H. Enoki, K. Sakaki, M. Seto, *J. Synchrotron Radiat.* **16**, 723 (2009).

[4] S. Yaroslavtsev, A.I. Chumakov, *J. Synchrotron Radiat.* **29**, 1329 (2022).

[5] A. Edström, M. Werwiński, D. Iuşan et al., *Phys. Rev. B* **92**, 174413 (2015).

[6] J. Marciniak, M. Werwiński, J. Rychły-Gruszecka, *J. Magn. Magn. Mater.* **589**, 171563 (2024).

[7] M. Strugatsky, K. Seleznyova, V. Zubov, J. Kliava, *Surf. Sci.* **668**, 80 (2018).

[8] V. Zayets, *AIP Adv.* **14**, 075309 (2024).

[9] H. Bunzel, E. Kreber, U. Gonser, *J. Phys. Colloq.* **35**, C6-609 (1974).

[10] T. Mitsui, Y. Imai, R. Masuda, M. Seto, K. Mibu, *J. Synchrotron Radiat.* **22**, 427 (2015).

[11] CrysAlisPRO, Oxford Diffraction/Agilent Technologies, Yarnton (UK).

[12] G.M. Sheldrick, *Acta Crystallogr. A* **71**, 3 (2015).

[13] S. Margulies, J.R. Ehrman, *Nucl. Instrum. Methods* **12**, 131 (1961).

[14] R.A. Brand, Normos Mössbauer Fitting Program, Wissel, 1987.

[15] T. Shinjo, F. Itoh, H. Takaki, *J. Phys. Soc. Jpn.* **19**, 1252 (1964).

[16] L. Takacs, M.C. Cadeville, I. Vincze, *J. Phys. F Mater. Phys.* **5**, 800 (1975).

[17] O.V. Zhdanova, M.B. Lyakhova, Y.G. Pastushenkov, *Met. Sci. Heat Treat.* **55**, 68 (2013).